Journal of Power Sources 196 (2011) 565–572

Contents lists available at ScienceDirect

Journal of Power Sources

journal homepage: www.elsevier.com/locate/jpowsour

Synthesis and electrochemical performance of multi-walled carbon nanotube/polyaniline/MnO_2 ternary coaxial nanostructures for supercapacitors

Qiang Li[a,b], Jianhua Liu[c], Jianhua Zou[c], Anindarupa Chunder[c], Yiqing Chen[b], Lei Zhai[c,*]

[a] School of Electronic Science and Applied Physics, Hefei University of Technology, Hefei, Anhui 230009, PR China
[b] School of Materials Science and Engineering, Hefei University of Technology, Hefei, Anhui 230009, PR China
[c] NanoScience Technology Center and Department of Chemistry, University of Central Florida, 12424 Research Parkway, Suite 400, Orlando, FL 32826, USA

ARTICLE INFO

Article history:
Received 23 April 2010
Received in revised form 22 June 2010
Accepted 23 June 2010
Available online 30 June 2010

Keywords:
Carbon nanotube
Polyaniline
Manganese oxide
Coaxial
Supercapacitor

ABSTRACT

Multi-walled carbon nanotube (MWCNT)/polyaniline (PANI)/MnO_2 (MPM) ternary coaxial structures are fabricated as supercapacitor electrodes via a simple wet chemical method. The electrostatic interaction between negative poly(4-styrenesulfonic acid) (PSS) molecules and positive Mn^{2+} ions causes the generation of MnO_2 nanostructures on MWCNT surfaces while the introduction of PANI layers with appropriate thickness on MWCNT surfaces facilitates the formation of MWCNT/PANI/MnO_2 ternary coaxial structures. The thickness of PANI coatings is controlled by tuning the aniline/MWCNT ratio. The effect of PANI thickness on the subsequent MnO_2 nanoflakes attachment onto MWCNTs, and the MPM structures is investigated by X-ray diffraction (XRD), X-ray photoelectron spectroscopy (XPS), transmission electron microscopy (TEM), and field-emission scanning electron microscopy (FESEM). The results suggest that appropriate thickness of PANI layers is important for building MPM ternary coaxial structures without the agglomeration of MnO_2 nanoflakes. The MPM ternary coaxial structures provide large interaction area between the MnO_2 nanoflakes and electrolyte, and improve the electrochemical utilization of the hydrous MnO_2, and decrease the contact resistance between MnO_2 and PANI layer coated MWCNTs, leading to intriguing electrochemical properties for the applications in supercapacitors such as a specific capacitance of 330 Fg^{-1} and good cycle stability.

Published by Elsevier B.V.

1. Introduction

Energy storage systems are playing important roles in storing energy generated from sun and wind, or other renewable energy sources [1–3]. Electrical energy storage systems include conventional capacitors, batteries, and electrochemical capacitors or supercapacitors. Supercapacitors are the primary choice for the applications where faster- and higher-power energy storage systems are needed because they have higher energy density than conventional capacitors, and higher power density and faster power delivery than batteries [2,3]. Supercapacitors are categorized into electrochemical double layer capacitors (EDLCs) and pseudo-capacitors depending on the charge storage mechanisms. Ion absorption of the electrical double layer at the electrode and electrolyte interface is the mechanism for charge storage in EDLCs which are usually built from carbon-based active materials with high surface area. Pseudo-capacitors store energy through fast and reversible redox reactions of transition metal oxides and electrical conductive polymers [1]. The active materials of EDLCs and pseudo-capacitors (i.e. carbon materials, conducting polymers and transition metal oxides) have their own advantages and disadvantages. Carbon materials, such as activated, graphitic, and carbide derived carbon, carbon fabrics, fibers, and nanotubes have outstanding electrical properties, long life-cycles and great mechanical properties, but low specific capacitance (5–200 Fg^{-1}) [4–10]. Conducting polymers are cost-effective and flexible, but have poor cyclability [11–13]. Among the transition metal oxides, MnO_2 is the most competitive candidate for supercapacitors due to its low cost, natural abundance, environmental safety, and very high theoretical specific capacitance (SC) of 1370 Fg^{-1} [14]. However, its intrinsically poor electronic conductivity and un-optimized morphology limit its practical capacitance at only one-fifth or one-sixth of the theoretical SC [15]. Binary or ternary composites of carbon materials, conducting polymers and MnO_2 have been investigated to utilize their advantages and overcome their disadvantages in supercapacitors. For example, carbon materials/conducting polymers [16–25], carbon materials/MnO_2 [26–30], conducting polymers/MnO_2 [31–34], and carbon materials/conducting polymers/MnO_2 [35–38] have been prepared as active materials for supercapacitor electrodes. CNT/poly(3,4-ethylenedioxythiophene) (PEDOT) [16], CNT/MnO_2 [29] and MnO_2/PEDOT [31] binary coaxial structures have been

* Corresponding author. Tel.: +1 407 882 2847; fax: +1 407 882 2819.
E-mail address: lzhai@mail.ucf.edu (L. Zhai).

0378-7753/$ – see front matter. Published by Elsevier B.V.
doi:10.1016/j.jpowsour.2010.06.073

fabricated, leading to exciting electrochemical performances. Ternary composites fabricated from poly(4-styrenesulfonic acid) (PSS) dispersed MWCNT, conducting polymers and MnO_2 with MnO_2 embedding in conducting polymer matrices have shown intriguing electrochemical properties and stability for supercapacitor applications [35,36]. These studies have demonstrated that larger interaction area among the active materials induced by nano-scale mixing can greatly improve their electrochemical performance. It is expected that decorating MnO_2 nanostructures on MWCNT/conducting polymer coaxial nanostructures would generate ternary coaxial structures with improved electrochemical utilization of MnO_2 by providing large interaction area between the active materials and electrolyte.

In this paper, we report the fabrication of MPM ternary coaxial structures through a cost-effective wet-chemical method and the investigation of their electrochemical properties as supercapacitor electrodes. In our studies, negatively charged PSS was used to stabilize the dispersed MWCNTs [39], as well as provide the electrostatic interaction to bind positive Mn^{2+} ions on MWCNT surfaces. Polyaniline (PANI) was deposited on PSS dispersed MWCNTs via the polymerization of aniline monomers in acid solutions to form MWCNT/PANI coaxial structures. Such MWCNT/PANI structures acted as templates for the subsequent synthesis of MnO_2 through the oxidation of Mn^{2+}, generating MnO_2 nanoflakes partially embedding in or sticking on to the templates. The resulted MPM ternary coaxial structures provided large interaction area between the MnO_2 nanoflakes and electrolyte to significantly improve the electrochemical utilization of the hydrous MnO_2 and decrease the contact resistance between MnO_2 and PANI layer coated MWCNTs, leading to intriguing electrochemical properties for the applications in supercapacitors such as a specific capacitance of 330 Fg^{-1} and volumetric capacitance of 296 Fcm^{-3}, and also good cycle stability.

2. Experimental

2.1. Fabrication of MWCNT/PANI/MnO_2 ternary composites

MWCNTs were purchased from Nanolab (Newton, MA) with a diameter of 10–20 nm and length about 5–20 μm. PSS, aniline, ammonium persulfate (APS), $Mn(CH_3COO)_2{\cdot}4H_2O$ and $KMnO_4$ were purchased from Sigma–Aldrich (St. Louis, MO) and used without further purification. Deionized (DI) water was used in all aqueous solutions. The MPM ternary composites were fabricated in two steps. The first step is to prepare MWCNT/PANI binary coaxial structures. 10 mg MWCNTs and 0.3 mL 18 wt% PSS were added to 10 mL DI water followed by 50 min sonication to disperse MWCNTs. Certain amount of 99.8% aniline monomers (25–100 μL) and 10 mL 1 M HCl aqueous solution were added to the PSS dispersed MWCNTs solution, and sonicated for 10 min. APS dissolved in 25 mL DI water was added dropwise into the above mixture in an ice bath for overnight under stirring. The prepared MWCNT/PANI composites were collected using centrifugation and washed with DI water through 3 sonication/centrifugation cycles. The second step is to prepare MPM ternary composites. The extracted fabricated MWCNT/PANI composites in the first step and 84.5 mg $Mn(CH_3COO)_2{\cdot}4H_2O$ were dissolved in 50 mL DI water, and then were stirred overnight. 37 mg $KMnO_4$ dissolved in 50 mL DI water was added dropwise into the solution and stirred for overnight. The fabricated MPM ternary composites were centrifuged and washed with DI water through 3 sonication/centrifugation cycles.

To examine the effect of the thickness of PANI layer coatings on the surface of MWCNTs on the structure and electrochemical performance of the MPM ternary composites, 0, 25, 50, 75 and 100 μL aniline monomers were used to synthesize PANI coatings on MWCNTs, respectively. The molar ratio of aniline monomers to APS is 1:2. The masses of MWCNTs, PSS, $Mn(CH_3COO)_2{\cdot}4H_2O$ and $KMnO_4$ and the volume of DI water were kept constant. The corresponding as-fabricated MPM ternary composites were marked as MPM0, MPM25, MPM50, MPM75 and MPM100 in the text, respectively.

2.2. Electrode preparation and characterization

5 mg MPM ternary composites were mixed with 5 μL Nafion (5 wt% in water) as a binder in 2 mL DI water by sonication and sprayed onto 1 cm × 1 cm surface of the graphite plates to build electrodes for supercapacitors. PSS dispersed MWCNTs were also used to make supercapacitor electrodes by the above method to be compared with MPM ternary composites. All electrodes were dried in a vacuum oven for 12 h at 80 °C. The masses of active materials were determined by weighting the graphite plates before and after spraying/drying. The nanostructures of the MPM ternary composites were examined using transmission electron microscopy (TEM) and high-resolution transmission electron microscopy (HRTEM). The crystal structure and chemical composition were analyzed using X-ray diffraction (XRD) and X-ray photoelectron spectroscopy (XPS), respectively. The surface morphologies of the prepared electrodes were examined using field-emission scanning electron microscopy (FESEM). CHI 660B electrochemical workstation was used to test the electrochemical performance of the electrodes. Electrochemical measurement was performed at room temperature in a three-electrode electrochemical system: a MPM ternary composite coated graphite plate as working electrode, a platinum plate as the counter electrode, and a saturated calomel electrode (Ag/AgCl) as the reference electrode. 0.5 M Na_2SO_4 solution was used as electrolyte, with N_2 purging for 10 min before the measurement.

3. Results and discussion

3.1. Material characterization

Fig. 1 shows the TEM images of the fabricated MPM ternary composites with different amounts of aniline (0, 25, 50, 75 and 100 μL corresponding to MPM0, MPM25, MPM50, MPM75 and MPM100, respectively.). Fig. 1a illustrates that MnO_2 nanoflakes with a size around 100 nm grew in bundles on the PSS dispersed MWCNTs (MPM0). In contrast, the size of MnO_2 nanoflakes on PANI coated MWCNTs (50 and 10 nm for sample MPM25 and MPM50, respectively.) is much smaller than that of MnO_2 nanoflakes on PSS dispersed MWCNTs (MPM0), suggesting an improved MnO_2/electrolyte interface attributed to PANI. The size of MnO_2 nanoflakes for MPM50 is determined from its HRTEM image in Fig. 2. Some bare MWCNTs are observed in the sample MPM25 and MPM50 probably due to the low aniline to MWCNT ratio. As the amount of aniline increased to 75 and 100 μL (MPM75 and MPM100), all MWCNTs are coated with PANI. However, no MnO_2 nanoflake is observed on the surfaces of PANI coated MWCNTs. Instead, MnO_2 nanoflakes with a size about tens of nanometers formed aggregates in solution. We believe that such phenomenon is caused by the PANI layers with different thickness in different samples. In our studies, MWCNTs were initially dispersed in DI water using negatively charged PSS, yielding a dispersion of individual MWCNTs stabilized by the static charge repulsion between PSS molecules [36]. The MnO_2 nanoflakes were synthesized by the following reactions [40,41]:

$$3Mn^{2+} + 2Mn^{7+} \rightarrow 5Mn^{4+}$$

$$Mn^{4+} + 2H_2O \rightarrow MnO_2 + 4H^+$$

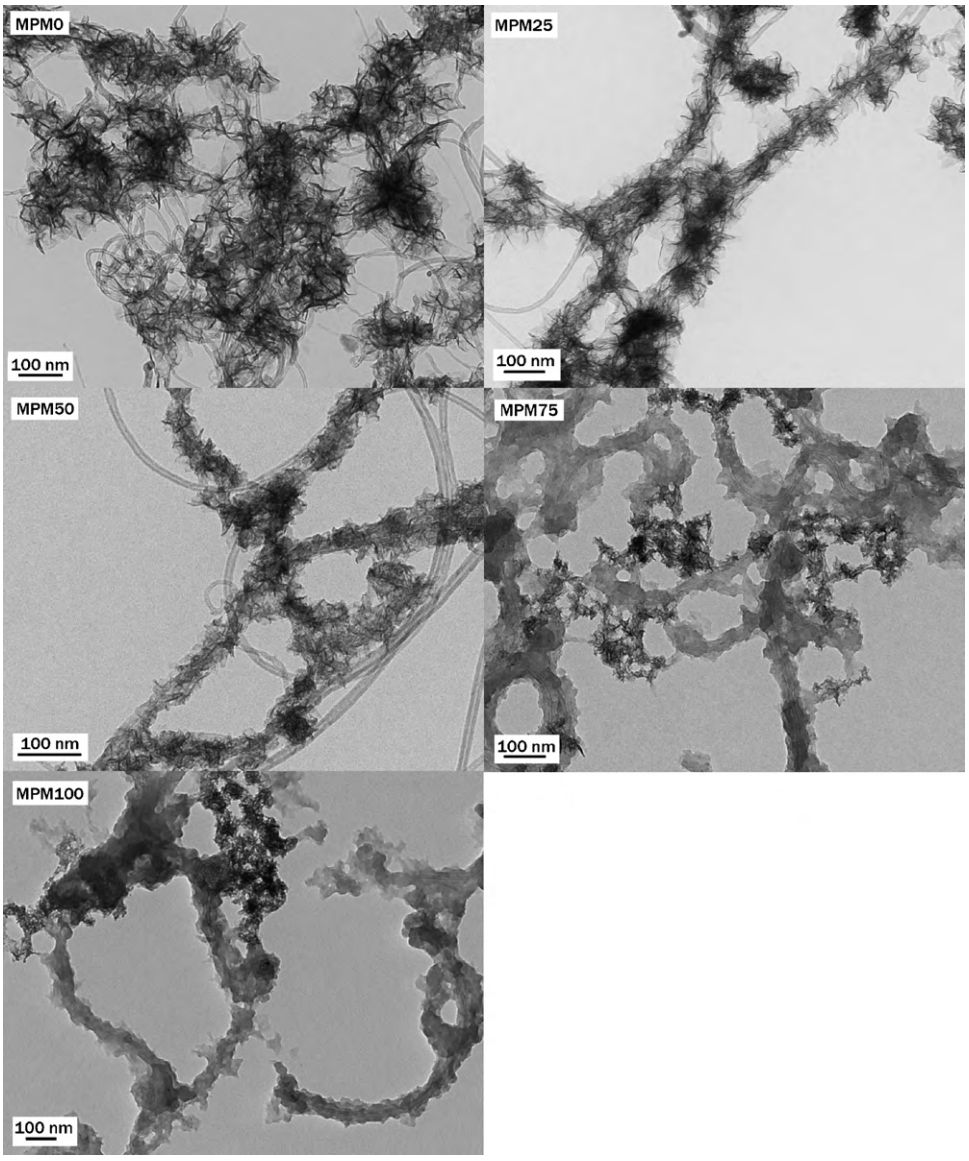

Fig. 1. TEM images of MPM0, MPM25, MPM50, MPM75, and MPM100.

When $Mn(CH_3COO)_2{\cdot}4H_2O$ was added to the solution of PSS dispersed MWCNTs without PANI coatings, the negative PSS molecules on the surface of MWCNTs would attract the positive Mn^{2+} ions through electrostatic interaction and function as the template for the formed MnO_2 nanoflakes. As a layer of PANI deposited on the PSS dispersed MWCNTs under acidic conditions, the positively charged PANI shielded the negatively charges on PSS, resulting in the reduction of electrostatic interaction on Mn^{2+} ions. Addi-

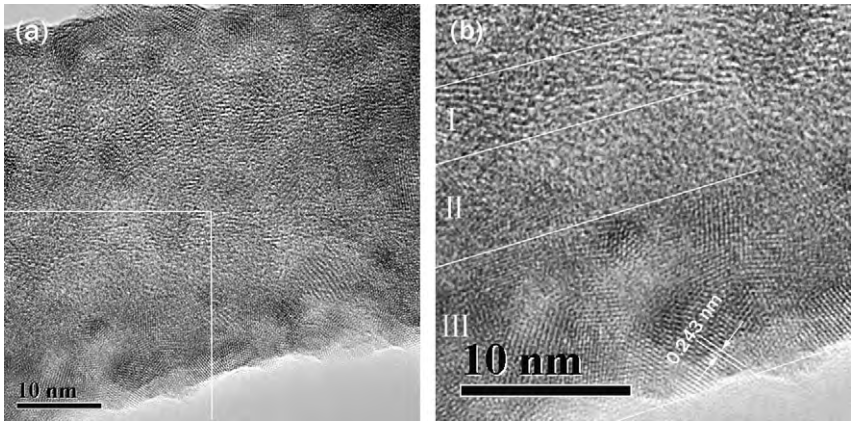

Fig. 2. (a) HRTEM image shows a MPM ternary coaxial structure of MPM50 and (b) higher magnification image of a selected square area in (a) showing three distinct regions: I, walls of MWCNT; II, a layer of PANI; III, a layer of MnO_2 nanoflakes.

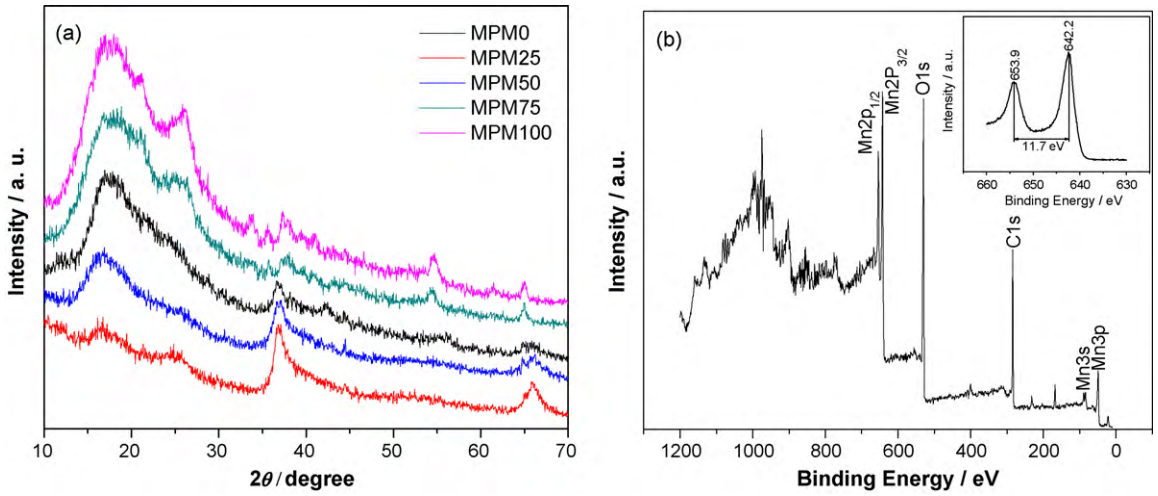

Fig. 3. (a) XRD patterns for MPM0, MPM25, MPM50, MPM75, and MPM100 and (b) XPS survey spectra of MPM50, the inset is the magnified spectrum of Mn 2p region.

tionally, the PANI layer can also separate PSS and Mn^{2+} ions and decrease the electrostatic interaction between them according to Coulomb's law of electric force [42]:

$$F = \frac{q_1 q_2}{r^2} \quad (1)$$

where F is the magnitude of the electric force, q_1 and q_2 are the charges of the two electronic objects, and r is the distance between the two objects. Due to these two possible reasons, the amount of PANI on PSS dispersed MWCNTs determines the absorption of Mn^{2+} ions on MWCNT surfaces. When a thin layer of PANI was deposited on PSS dispersed MWCNTs, Mn^{2+} ions were attracted to the surface and turned into MnO_2 nanoflakes embedding in or sticking on the PANI layer upon the oxidation of $KMnO_4$, forming the MPM ternary coaxial nanostructures (MPM25 and MPM50). In contrast, a thick layer PANI on PSS dispersed MWCNTs would diminish the electrostatic attraction between PSS molecules and Mn^{2+} ions, causing the formation of MnO_2 nanoflakes in solutions (MPM75 and MPM100).

Detailed structural information for sample MPM50 was examined using a high-resolution transmission electron microscope (HRTEM) since it had the best ternary coaxial structures. Fig. 2a is the HRTEM image of the ternary coaxial structure. Higher magnification image (Fig. 2b) of a selected square area in Fig. 2a illustrates three distinct regions (I, II, and III) representing the walls of MWCNT, a layer of PANI, and MnO_2 nanoflakes decorating the PANI layer, respectively. The size of MnO_2 nanoflakes is less than 10 nm with a distance of 0.243 nm between the neighboring lattice fringes, corresponding to the d-spacing (0.244 nm) of the (0 0 6) plane in birnessite MnO_2.

The crystal structures of the composites were studied using X-ray diffraction (XRD) and the patterns are presented in Fig. 3a. The diffraction peaks of MPM0, MPM25, and MPM50 are assigned to those of birnessite MnO_2 with cell parameters of $\alpha = b = 5.82$ Å, $c = 14.62$ Å (JCPDS 18-0802). The diffraction patterns vary with different samples probably because of the orientation of MnO_2 nanoflakes. For example, the diffraction peaks located at 42.6° and 55.1° in the diffraction pattern of sample MPM0 are not visible in the diffraction patterns of sample MPM25 and MPM50, while the diffraction peaks located at 36.8° and 65.7° become stronger in the diffraction patterns of MPM25 and MPM50. Such difference is also illustrated in the HRTEM image (Fig. 2b) where most MnO_2 nanoflakes have a d-spacing of 2.43 Å ((0 0 6) plane in birnessite MnO_2), corresponding to the diffraction peak at 36.8° in XRD. The diffraction peaks of MPM75 and MPM100 can match those of the above birnessite MnO_2 (JCPDS 18-0802) with small deviations possibly caused by the dense PANI around MnO_2 nanoflakes. The peak at 26° could be ascribed to the (0 0 2) plane diffraction of MWCNTs [43], and the peak at 20.8° for MPM75 and MPM100 corresponds to the (0 2 0) plane of PANI in its emeraldine salt form [44,45]. The broad peak positioned at about 17° is caused by the tape used to fix the composites for XRD examination. The surface chemical composition of sample MPM50 was investigated by X-ray photoelectron spectroscopy (XPS). The spectrum in Fig. 3b illustrates the existence of manganese by peaks assigned to manganese Mn $2p_{3/2}$ and its satellite peaks of Mn $2p_{1/2}$, Mn 3s and Mn 3p. The binding energies of Mn $2p_{3/2}$ (642.2 eV) and Mn $2p_{1/2}$ (653.9 eV) and their spin energy difference (11.7 eV) are consistent with the Mn $2p_{3/2}$ and Mn $2p_{1/2}$ in MnO_2 (inset Fig. 2b) [46].

3.2. Electrochemical characterization

MPM0, MPM25, MPM50, MPM75 and MPM100 were dispersed with binder in DI water and sprayed on the surface of graphite plates to build electrodes for supercapacitors. The surface morphologies of the electrodes fabricated from these five as-fabricated materials were characterized by FESEM (Fig. 4). It is observed that the electrodes fabricated from sample MPM0 and MPM25, MPM50 have porous surface structures, while those made from MPM75 and MPM100 have a rough dense morphology probably because of large amount of aniline used to form PANI. The inset of panel MPM100 in Fig. 4 clearly shows the underneath MWCNTs in the cracks formed by the shrinking of active materials on the surface of electrodes. Fig. 4 also demonstrates that the PSS dispersed MWCNTs are embedded in MnO_2 nanoflakes agglomerates for the electrodes made from MPM0. In contrast, the surface of the electrodes made from MPM25 and MPM50 is mainly consisted of individual MPM coaxial nanowires. These different surface morphologies of the electrodes built from different composites will induce different electrochemical performances as discussed in the following part.

Cyclic voltammetry (CV) examinations of all fabricated electrodes were performed in a potential window from −0.2 to 0.8 V (vs AgCl/Ag) at different scan rates using three-electrode system in 0.5 M Na_2SO_4 solutions. The specific capacitance was calculated from CV curves according to the following equation:

$$C = \frac{I}{m\nu} \quad (2)$$

where I is the current, m is the mass of reactive material, and ν is the potential scan rate. The CV curves of all fabricated electrodes at a potential scan rate of 5 mVs^{-1} are shown in Fig. 5a. The MPM50 has the highest specific capacitance of 330 Fg^{-1} and volumetric capaci-

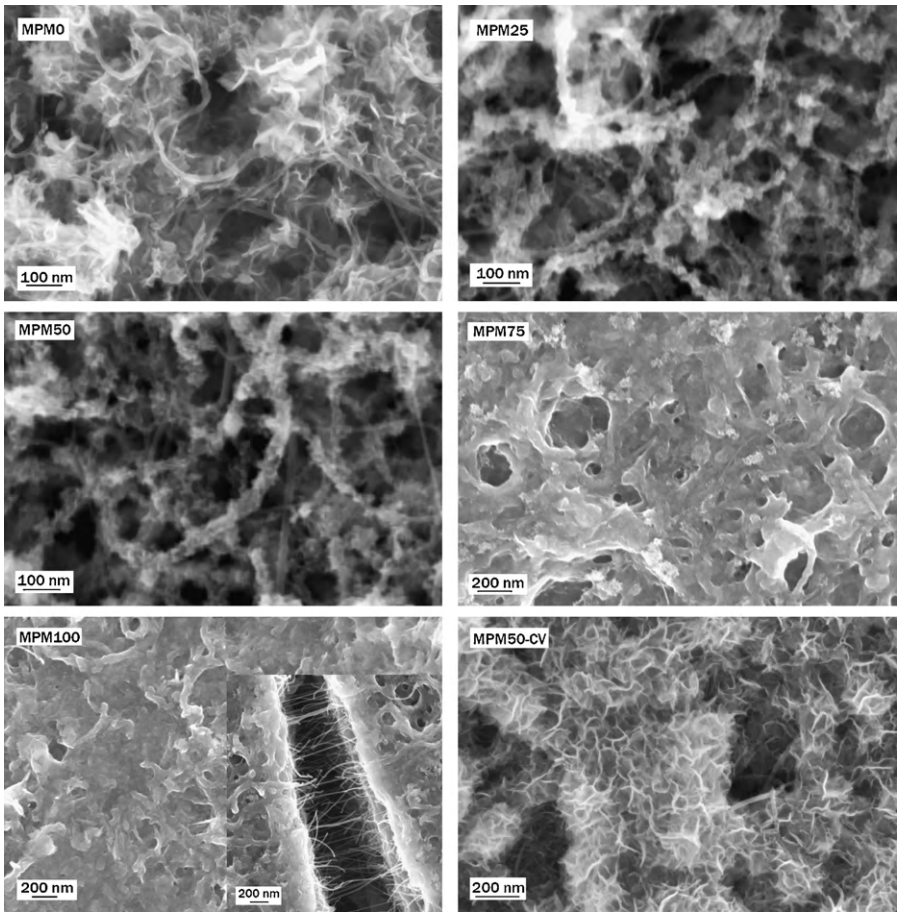

Fig. 4. SEM images of the electrodes prepared from MPM0, MPM25, MPM50, MPM75, and MPM100 and the MPM50-CV (MPM50 after 1000 life-cycles at a potential scan rate of 20 mVs^{-1}). The inset in MPM100 shows a crack on the surface of the electrode.

tance of 296 Fcm^{-3} among the five samples, which also much higher than those of PSS dispersed MWCNTs (15 Fg^{-1} and 21 Fcm^{-3}). The CV curves of MPM0, MPM25, and MPM50 are relatively rectangular in shape with two weak redox peaks, suggesting that their capacitance is attributed to the charging/discharging process happened at the interface between electrolyte and MnO_2 nanoflakes following the pseudocapacitive charge storage mechanism [40]. The MnO_2 pseudocapacitance in aqueous media is usually generated by the transitions of interfacial oxycation species at various oxidation states, and the redox peaks may reflect the redox transitions of manganese between different valence states, including Mn^{3+}/Mn^{2+}, Mn^{4+}/Mn^{3+}, and Mn^{6+}/Mn^{4+} [47,48]. Therefore, energy extracted from a MnO_2 electrode strongly depends on the quality of MnO_2/electrolyte and MnO_2/current collector interfaces. The aggregates of MnO_2 nanoflakes in MPM0 not only hinder the electrolyte ions from reaching MnO_2 nanoflake inner structures, but also cause the high contact resistance between MWCNTs and MnO_2 nanoflakes, resulting in the equivalent series resistance (ESR) as high as 76 Ω [36]. In contrast, the MPM coaxial nanostructures in MPM25 and MPM50 have improved dispersion of MnO_2 nanoflakes in the MWCNT/PANI matrix, and effectively enhance the electrochemical utilization of MnO_2 nanoflakes. Electrical conductivity of active materials is also improved (the ESR is about 8 Ω) by larger interconnected area between MnO_2 nanoflakes and conducting PANI coating on the surface of MWCNTs. The thin PANI layer on MWCNTs functions as an electronically conductive matrix for MnO_2 nanoflakes, and partially contributes the specific capacitance. The TEM images in Fig. 2 show that MnO_2 nanoflakes in MPM50 is smaller than those in MPM25, suggesting a more efficient electrochemical utilization of MnO_2 nanoflakes in MPM50. Such structural impact on the electrochemical performance is clearly illustrated by the specific capacitance difference between MPM50 and MPM25 at potential scan rate of 5 mVs^{-1}. The specific capacitances of MPM75 and MPM100 are almost the same, and much lower than that of sample MPM0, suggesting that MnO_2 nanoflakes in MPM75 and MPM100 contributes little to their specific capacitances. Such poor electrochemical performance is due to the thick PANI (as shown in Fig. 4 MPM75 and MPM100) that limits the effective utilization of active materials [17,49,50].

Fig. 5b shows the specific capacitances of all fabricated electrodes at different potential scan rates. Generally, the specific capacitance decreases with the increase of potential scan rate because the electrolyte ions only reach the outer surface of the electrode at high scan rates, and the active material that is accessible only through the deep pores does not actively contribute to the pseudocapacitance [35]. The small change of the specific capacitance for MPM0, MPM75 and MPM100 suggests that these samples have less porous structures than MPM25 and MPM50. Fig. 5c shows the CV responses of MPM50 at different potential scan rates. The CV curves at 5, 10, and 20 mVs^{-1} are relatively in the rectangular shape with two weak redox peaks. The cathodic peaks shift positively and the anodic peaks shift negatively with the increase of potential scan rates form 5 to 20 mVs^{-1} is due to the resistance of the electrode [45,51].

The cycling stability of the electrode fabricated from MPM50 was tested by CV at a potential scan rate of 20 mVs^{-1} for 1000 life-cycles. Fig. 6a shows the voltammograms recorded for the 1st, 100th, and 1000th cycle. The specific capacitance decreases to 79%

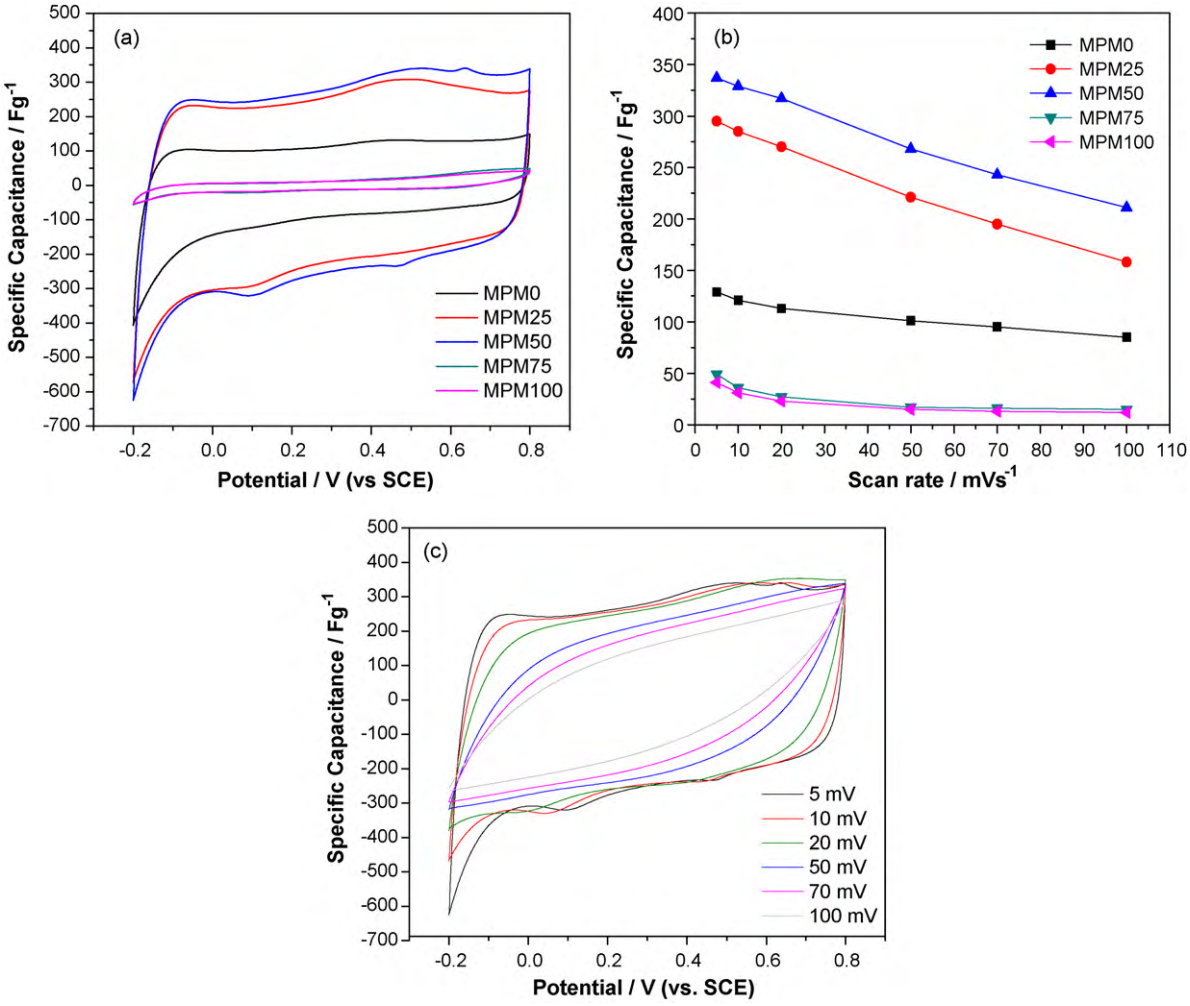

Fig. 5. (a) Cyclic voltammograms of electrodes fabricated from MPM0, MPM25, MPM50, MPM75, and MPM100 at a potential scan rate of 5 mVs^{-1}; (b) specific capacitance of the electrodes as a function of scan rates and (c) cyclic voltammograms of the electrode fabricated from MPM50 at various scan rates.

of the original value after 100 cycles and remains 77% of the original value after 1000 cycles. The decrease of the specific capacitance is probably due to the evolution of the MnO_2 nanostructures during the voltammograms cycle. The SEM image of the electrode fabricated from MPM50 after 1000 voltammogram cycles (MPM50-CV in Fig. 4) clearly shows that the material morphology changes from coaxial structures to petal-like structures with larger crystal size and reduced interfacial area with PANI and MWCNTs. Such mor-

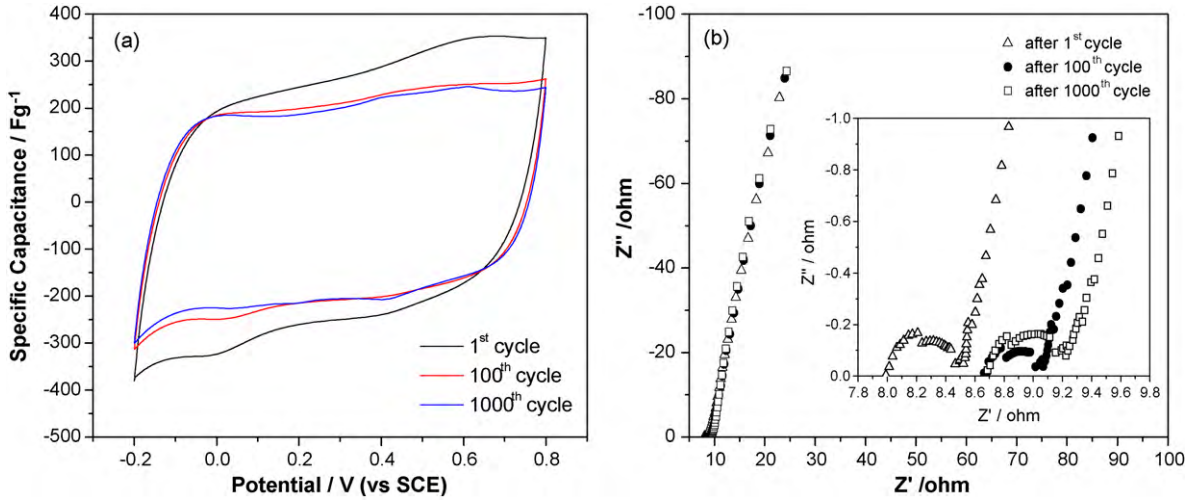

Fig. 6. (a) Cyclic voltammograms of the electrode fabricated from MPM50 after the 1st, 100th, and 1000th cycles at a potential scan rate of 20 mVs^{-1} and (b) Nyquist plots of the electrode after the 1st, 100th, and 1000th cycles.

phology change is believed to follow a dissolution–redeposition mechanism. As the applied potential is scanned from −0.2 to 0.8 V (vs SCE), the MnO_2 nanocrystals on MWCNTs are reduced and some of the reduce manganese is dissolved into the electrolyte as Mn^{2+} cations. During forward cycling, MnO_2 is formed from the dissolved Mn^{2+} cations through the oxidation and redeposits on the electrode surface. By repeating such redox process, MnO_2 oxide nanocrystals dissolve and redeposit to form petal-like nanosheets. The resulted larger MnO_2 crystals have detrimental impact on the MnO_2/current collector and MnO_2/electrolyte interfaces which will reduce the electrode capacitance and increase the ESR [52].

The electrochemical impedance of the electrode after 1st, 100th, and 1000th cycle were examined over the frequency range of 10 kHz–10 MHz at a dc bias of 0 V with a sinusoidal signal of 5 mV, as shown in Fig. 6b. A semicircular loop in high frequency followed by a nearly vertical straight line in the low frequency is observed after 1st, 100th, and 1000th cycle. The capacitive behaviors start from 69.8 Hz, suggesting a good capacitive respond of sample MPM50 attributed to a fast charge/discharge process [17]. The ESR increased from 7.95 Ω after 1st cycle to 8.65 Ω after 100th cycle, and remains the same value up to 1000th cycle. The ESR is consisted of the uncompensated electrical resistance of the active materials (R_Ω), the electrolyte resistance (R_e) and the electrical leads (R_l). The increase of ESR is mainly due to the increase of the R_Ω because the R_e and R_l remain the same in the charge/discharge process [17,53]. The increase of ESR may be caused by the contact resistance between active materials and the graphite substrate due to the increase of MnO_2 crystal size. The control of material morphology evolution is important to obtain high capacitance and elongate electrode lifetime. The relationship between operation parameters such as scan rate and material morphology evolutions is under current investigation.

4. Conclusions

Multi-walled carbon nanotube (MWCNT)/polyaniline (PANI)/MnO_2 (MPM) ternary coaxial nanostructures are fabricated via a simple wet chemical method. The electrostatic interaction between negative poly(4-styrenesulfonic acid) (PSS) molecules and positive Mn^{2+} ions facilitates the formation of MnO_2 nanostructures on MWCNTs. The thickness of PANI coating on MWCNTs is controlled by tuning the aniline/MWCNT ratio. The investigation of the effect of PANI thickness on the subsequent MnO_2 nanoflakes attachment onto MWCNTs, and the MPM structures suggests that the interaction between PSS and Mn^{2+} ions is necessary to build MPM ternary coaxial nanostructures. The comparison of electrochemical properties of MWCNT/MnO_2 composites (MPM0), MWCNT/PANI/MnO_2 ternary coaxial composites (MPM25 and MPM50) and MWCNT/PANI composites with MnO_2 nanoflakes (MPM75 and MPM100) suggests that MWCNT/PANI/MnO_2 ternary coaxial composites provide large interaction area between the MnO_2 nanoflakes and electrolyte to improve the electrochemical utilization of the hydrous MnO_2, as well as decrease the contact resistance between MnO_2 and PANI layer coated MWCNTs, leading to intriguing electrochemical properties for the applications in supercapacitors. The studies of the electrode cycling stability indicate that controlling the evolution of material morphology is important to obtain high capacitance and elongate electrode lifetime.

Acknowledgements

The authors are grateful to Dr. Diego J. Diaz, Dr. Qi Zhang and Kirk Scammon for their help. The support provided by China Scholarship Council (No. 2009104389) during a visit of Qiang Li to the University of Central Florida, the characterization support from Material Characterization Facility at the University of Central Florida and the financial support from National Science Foundation CAREER award DMR 0746499 are gratefully acknowledged.

References

[1] P. Simon, Y. Gogotsi, Nat. Mater. 7 (2008) 845–854.
[2] B.E. Conway, Electrochemical Supercapacitors: Scientific Fundamentals and Technological Applications, Plenum Publishers, New York, 1999.
[3] J.R. Miller, P. Simon, Science 321 (2008) 651–652.
[4] J. Gamby, P.L. Taberna, P. Simon, J.F. Fauvarque, M. Chesneau, J. Power Sources 101 (2001) 109–116.
[5] D.H. Jurcakova, X. Li, Z.H. Zhu, R.D. Marco, G.Q. Lu, Energy & Fuels 22 (2008) 4139–4145.
[6] M. Arulepp, J. Leis, M. Lätt, F. Miller, K. Rumma, E. Lust, A.F. Burke, J. Power Sources 162 (2006) 1460–1466.
[7] K. Hung, C. Masarapu, T. Ko, B.Q. Wei, J. Power Sources 193 (2009) 944–949.
[8] C. Portet, J. Chmiola, Y. Gogotsi, S. Park, K. Lian, Electrochim. Acta 53 (2008) 7675–7680.
[9] C.M. Yang, Y.J. Kim, M. Endo, H. Kanoh, M. Yudasaka, S. Iijima, K. Kaneko, J. Am. Chem. Soc. 129 (2007) 20–21.
[10] D.W. Wang, F. Li, M. Liu, G.Q. Lu, H.M. Cheng, Angew. Chem. Int. Ed. 47 (2008) 373–376.
[11] K.S. Ryu, K.M. Kim, N.G. Park, Y.J. Park, S.H. Chang, J. Power Sources 103 (2002) 305–309.
[12] L.Z. Fan, J. Maier, Electrochem. Commun. 8 (2006) 937–940.
[13] B. Muthulakshmi, D. Kalpana, S. Pitchumani, N.G. Renganathan, J. Power Sources 158 (2006) 1533–1537.
[14] M. Toupin, T. Brousse, D. Bélanger, Chem. Mater. 16 (2004) 3184–3190.
[15] M. Toupin, T. Brousse, D. Bélanger, Chem. Mater. 14 (2002) 3946–3952.
[16] L. Chen, C.Z. Yuan, H. Dou, B. Gao, S.Y. Chen, X.G. Zhang, Electrochim. Acta 54 (2009) 2335–2341.
[17] S.R. Sivakkumar, W.J. Kim, J.A. Choi, D.R. MacFarlane, M. Forsyth, D.W. Kim, J. Power Sources 171 (2007) 1062–1068.
[18] Y.P. Fang, J.W. Liu, D.J. Yu, J.P. Wicksted, K. Kalkan, C.O. Topal, B.N. Flanders, J. Wu, J. Li, J. Power Sources 195 (2010) 674–679.
[19] D.W. Wang, F. Li, J.P. Zhao, W.C. Ren, Z.G. Chen, J. Tan, Z.S. Wu, I. Gentle, G.Q. Lu, H.M. Cheng, ACS Nano 3 (2009) 1745–1752.
[20] L.P. Zheng, Y. Wang, X.Y. Wang, N. Li, H.F. An, H.J. Chen, J. Guo, J. Power Sources 195 (2010) 1747–1752.
[21] H.L. Wang, Q.L. Hao, X.J. Yang, L.D. Lu, X. Wang, Electrochem. Commun. 11 (2009) 1158–1161.
[22] K. Zhang, L.L. Zhang, X.S. Zhao, J.S. Wu, Chem. Mater. 22 (2010) 1392–1401.
[23] L.X. Li, H.H. Song, Q.C. Zhang, J.Y. Yao, X.H. Chen, J. Power Sources 187 (2009) 268–274.
[24] L.Z. Fan, Y.S. Hu, J. Maier, P. Adelhelm, B. Smarsly, M. Antonietti, Adv. Funct. Mater. 17 (2007) 3083–3087.
[25] A. Laforgue, P. Simon, J.F. Fauvarque, M. Mastragostino, F. Soavi, J.F. Sarrau, P. Lailler, M. Conte, E. Rossi, S. Saguatti, J. Electrochem. Soc. 150 (2003) A645–A651.
[26] G.R. Li, Z.P. Feng, Y.N. Ou, D.C. Wu, R.W. Fu, Y.X. Tong, Langmuir 26 (2010) 2209–2213.
[27] R.R. Jiang, T. Huang, Y. Tang, J.L. Liu, L.G. Xue, J.H. Zhuang, A.S. Yu, Electrochim. Acta 54 (2009) 7173–7179.
[28] J. Yan, Z.J. Fan, T. Wei, J. Cheng, B. Shao, K. Wang, L.P. Song, M.L. Zhang, J. Power Sources 194 (2009) 1202–1207.
[29] A.L.M. Reddy, M.M. Shaijumon, S.R. Gowda, P.M. Ajayan, J. Phys. Chem. C 114 (2010) 658–663.
[30] Y. Chen, C.G. Liu, C. Liu, G.Q. Lu, H.M. Cheng, Mater. Res. Bull. 42 (2007) 1935–1941.
[31] R. Liu, S.B. Lee, J. Am. Chem. Soc. 130 (2008) 2942–2943.
[32] K.T. Lee, J.F. Lee, N.L. Wu, Electrochim. Acta 54 (2009) 6148–6153.
[33] M. Nakayama, Y. Kashiwa, K. Suzuki, J. Electrochem. Soc. 156 (2009) D125–D130.
[34] E.C. Rios, A.V. Rosario, R.M.Q. Mello, L. Micaroni, J. Power Sources 163 (2007) 1137–1142.
[35] R.K. Sharma, L. Zhai, Electrochim. Acta 54 (2009) 7148–7155.
[36] R.K. Sharma, A. Karakoti, S. Seal, L. Zhai, J. Power Sources 195 (2010) 1256–1262.
[37] C.Z. Yuan, L.H. Su, B. Gao, X.G. Zhang, Electrochim. Acta 53 (2008) 7039–7047.
[38] S.R. Sivakkumar, J.M. Ko, D.Y. Kim, B.C. Kim, G.G. Wallace, Electrochem. Acta 52 (2007) 7377–7385.
[39] C. Duarte, M.A. Sobal, N.L. Marzan, L.M. Giersig, Adv. Mater. 16 (2004) 2179–2184.
[40] R.K. Sharma, H.S. Oh, Y.G. Shul, H.S. Kim, J. Power Sources 173 (2007) 1024–1028.
[41] S. Devaraj, N. Munichandariah, J. Electrochem. Soc. 154 (2007) A80–A88.
[42] K.W. Ford, Classical and Modern Physics, Xerox College Publishing, Lexington, Massachusetts, 1973.
[43] Z.S. Lou, Q.W. Chen, W. Wang, Y.F. Zhang, Carbon 41 (2003) 3063–3074.
[44] H.K. Chaudhari, D.S. Kelkar, Polym. Int. 42 (1997) 380–384.
[45] J. Yan, T. Wei, Z.J. Fan, W.Z. Qian, M.L. Zhang, X.D. Shen, F. Wei, J. Power Sources 195 (2010) 3041–3045.

[46] C.D. Wanger, W.M. Riggs, L.E. Davis, J.F. Moulder, G.E. Muilenberg, Handbook of X-ray Photoelectron Spectroscopy, Perkin-Elmer, Eden Prairie, 1978.
[47] O. Ghodbane, J.L. Pascal, F. Favier, ACS Appl. Mater. Interfaces 1 (2009) 1130–1139.
[48] C.C. Hu, T.W. Tsou, Electrochem. Commun. 4 (2002) 105–109.
[49] J. Zhang, L.B. Kong, B. Wang, Y.C. Luo, L. Kang, Synth. Met. 159 (2009) 260–266.
[50] Y.W. Lin, H.H. Chang, Y.S. Liu, M.C. Tsai, Y.C. Tsai, T.M. Wu, J. Electrochem. Soc. 157 (2010) K15–K20.
[51] Y.G. Wang, H.Q. Li, Y.Y. Xia, Adv. Mater. 18 (2006) 2619–2623.
[52] W. Wei, X. Cui, W. Chen, D.G. Ivey, Electrochim. Acta 54 (2009) 2271–2275.
[53] C.J. Wen, C. Ho, B.A. Boukamp, I.D. Raistrick, W. Weppner, R.A. Huggins, Int. Met. Rev. 26 (1981) 253–268.